Mixed Ionic and Electronic Conducting Ultra-Thin Lithium Silicide Interlayer for Solid-State Lithium Batteries

Jaekyung Sung[1,2], So Yeon Kim[1,2], Avetik Harutyunyan[3], Maedeh Amirmaleki[1,2], Sookyung Jeong[4], Yoonkwang Lee[5], Yeonguk Son[6], Ju Li[1,2]*.

[1]Department of Nuclear Science and Engineering, Massachusetts Institute of Technology, Cambridge, MA, USA

[2]Department of Materials Science and Engineering, Massachusetts Institute of Technology, Cambridge, MA, USA

[3]Honda Research Institute USA, San Jose, CA, USA

[4]Cell Design and Development Team, Rivian, Irvine, CA, USA

[5]Advanced Battery Development Team, Hyundai Motor Company, Hwaseong, 18280 Republic of Korea

[6]Department of Chemical Engineering, Changwon National University, Changwon, Gyeongsangnam-do 51140, Republic of Korea

E-mail: liju@mit.edu

Abstract

All-solid-state batteries using metallic lithium are regarded as a feasible next-generation energy storage system with high safety and energy density. However, the unstable interface originating from the decomposition of solid-state-electrolyte and dendritic lithium formation (issues of electrochemical and mechanical stability) hinders their feasible application. Herein, we demonstrate an ultra-thin interlayer design (~3.25 μm) of lithium silicide-carbon nanotubes (which have a property of mixed ionic and electronic conductor, MIEC) synthesized by electrochemical and non-electrochemical lithiation using the low-priced ingredient of silicon. Its features of 1) thermodynamically and electrochemically stable lithium silicide, not leading to decomposition of solid-state-electrolytes; 2) high lithiophilicity; and 3) large amounts of active sites offering 3-dimensional contact for lithium nucleation-- all contribute to the highly reversible plating/stripping upon repeated cycling without by-product formation and dendritic lithium. In addition, because of small-sized pores inducing mitigation of stress intensification inside the interlayer and reinforced mechanical strength by adding carbon nanotubes, the interlayer sustains its morphological integrity without any short-circuiting issues. As a result, a full-cell configuration containing nickel-rich layered cathode material, sulfide-based argyrodite solid-state-electrolyte (Li_6PS_5Cl), and metallic lithium for lithiation of silicon nanoparticles-carbon nanotubes interlayer displays high specific capacity (207.8 mAh g^{-1}), initial Coulombic efficiency (92.0%), capacity retention ratio of 88.9% after 200 cycles (Coulombic efficiency reaches 99.9% after tens of cycles), and rate capability (75% at 5C).

Context & Scale

For the satisfaction of ever-increasing energy demands, many researchers have been seeking state-of-the-art materials and systems for lithium-based secondary batteries. The use of the lithium metal anode with theoretical capacity (3,860 mAh g^{-1}) has been considered as rising star for next-generation anodes to replace with the conventional graphite anode (372 mAh g^{-1}). However, fatal safety issues, which comes from the penetration (short-circuiting) of soft separator by unstable dendritic lithium formation and flammable liquid-state electrolyte in current battery system, encourage battery community to explore the solid-state-electrolyte. Despite of its competitive properties of solid-based batteries, unstable interface between the lithium and solid-state-electrolyte remains to be solved for a feasible battery. In this work, we propose a new and feasible design of mixed ionic and electronic conducting interlayer using lithium silicide-carbon nanotubes in all-solid-state batteries. It allows lithium to uniformly deposit as well as prevents decomposition of an argyrodite-based solid-electrolyte, which gives rise to stable interface without any short-circuiting issues and excellent cycle life (88.9% after 200 cycles).

Introduction

As the electric vehicle (EV) market is rapidly increasing, the demand for lithium-ion batteries (LIBs) with safe and high energy density is growing more and more[1-3]. To overcome the low theoretical capacity of graphite (372 mAh g^{-1}) in LIBs, attempts have been made to use metallic lithium in the body-centered cubic (Li_{BCC}) crystal structure as an anode material because of its high theoretical specific capacity (3,860 mAh g^{-1}) and lowest reduction potential (−3.04 V versus standard hydrogen electrode)[4-6]. However, dendritic lithium (Li) formation for the plating/stripping process can penetrate through a separator, bringing about battery short-circuiting, and eventually fire and explosion[7,8]. Commercially available LIB systems using liquid-state electrolytes with features of flammability and volatility further accelerate fatal safety issues[9,10]. Accordingly, adopting all-solid-state batteries (ASSBs) has attracted much attention in consequence of their outstanding properties. Solid-state-electrolytes with low flammability have much less risk of ignition and explosion as well as mechanical stability, alleviating the internal short-circuiting issues by suppressing the dendritic Li growth[11,12]. High thermal stability, which enables the elimination of heavy and large thermal management systems, and availability of bipolar stacking configuration at a cell level, further improve the energy density of a battery pack for EVs[13,14].

Among a wide range of solid-state-electrolytes, inorganic (ceramic/glass) solid-state-electrolytes have been widely studied owing to their better mechanical properties than polymer electrolytes[15]. In particular, sulfide-based argyrodite solid-state-electrolytes have captivated researchers in the battery community because they feature high ionic conductivity of 10^{-2}–10^{-4} S cm^{-1} and ductility that enables fabrication of densified electrodes on a large scale via a simple roll-to-roll slurry coating and calendering process[16-18] (Oxide-based electrolytes require a high-temperature sintering process, which is limitation to the scalable synthesis). That being said, intrinsic properties of reductive decomposition coming from its narrow electrochemical stability window and thermodynamic instability at the interface of the sulfide-based electrolytes with Li_{BCC} still remain to be addressed[19-21]. The formation of a series of by-products (Li_2S, Li_3P, and LiCl) with poor ionic conductivity and their volumetric variation gives rise to a large increase in interfacial resistance. This decomposition keeps causing the growth of the reduction layer contributing to fracture formation in the solid-separator; and then Li deposited along these cracks further leads to stress intensification upon repeated cycles, which eventually results in internal short-circuiting. To address these concerns, various strategies, such as hybrid electrolytes[22] (Li_6PS_5Cl/poly(ethylene oxide) composite), alloys[23-25] (In-Li and Ag-Li), and interlayers[26-31] (e.g., polymer with Li salt, graphite, and Ag-C layer), have been proposed to prevent the direct contact of Li and electrolytes. Among them, interlayer design has advantages with prevention of direct contact between the solid-separator and Li as well as a simple fabrication process. The previous Ag-C interlayer has manifested outstanding cycling stability through the high lithiophilicity of Ag resulting in the formation of

reversible dense Li. Nevertheless, the use of costly ingredients of noble metal, which hinders commercial feasibility, needs to be replaced with cost-effective elements, and therefore further comprehensive and fundamental consideration to develop the sophisticated interlayer design is necessary.

A material for an interlayer that is thermodynamically stable in contact with both Li_{BCC} and solid-state-electrolytes should be identified. A wide range of electrochemical windows is also one of the crucial factors for preventing the unwanted formation of solid-electrolyte-interphase. Since electrochemically generated mechanical stresses coming from Li fingers would fracture the interlayer, they should be mitigated at the step of Li nucleation and by creeping of Li_{BCC}. For these reasons, we believe that an interlayer material has to have features including high lithiophilicity and high surface area with 3-dimensional (3D) structure that is capable of offering numerous active sites (which is a high true contact area) for stable Li_{BCC} nucleation upon the initial step of lithiation[32,33]. For high Li reversibility during (de)lithiation, the interlayer should also have characteristics of mixed ionic and electronic conductor (MIEC) as a prerequisite[34,35]. When it comes to the material characteristics of Li_{BCC}, the homologous temperature for Li_{BCC} is $T/T_M = 0.66$ (the melting point of Li_{BCC} is TM = 180 °C) and it has the property of being a soft metal. Besides, it shows a significant creep strain rate $\varepsilon(T, \sigma)$ (where σ is the deviatoric shear stress) by dislocation power-law creep or diffusional creep mechanisms suggesting that the Li_{BCC} may behave like an 'incompressible work fluid' during battery cycling[35-37]. A noticeable feature is that the diffusive processes mediating Coble diffusion softening is dominant at a very small sample size, finally leading fact that the normal ''smaller is stronger'' trend is changed to ''smaller is much weaker'' (Figure 1a)[38]. That is to say, the small-sized void space in the 3D interlayer helps to relieve the stresses (hydrostatic and deviatoric), so therefore both solid-state-electrolytes and interlayer can sustain their morphological integrity. In addition, high mechanical strength is demanded for the interlayer itself when also considering extreme pressure during the fabrication of ASSBs. With the satisfaction of the above critical parameters, the thickness of the MIEC interlayer should be minimized for high energy density. Herein, we propose a MIEC design of ultra-thin hybrid lithium silicide (LiSi)-carbon nanotubes (CNTs) interlayer (denoted to LiSi-C) through lithiation of cheap silicon (Si) as shown in schematic illustration of Figure 1b. Interesting phenomenon is that compressive stresses of massive Si volume expansion (which was well-known root cause of capacity degradation in LIBs) and the soft nature of LiSi help to improve the adhesion with solid-separator. We therefore obtained stable reversible plating/stripping behavior on current collector in asymetric solid-state cell configuration using sulfide-based argyrodite (Li_6PS_5Cl). A full-cell containing NCM811 cathode achieved excellent cycling stability (97.65% after 49 cycles) even at low operating temperature of 20 °C.

Results and discussion

Fabrication of LiSi-C interlayer. We first prepared the commercial Si nanoparticles (SiNPs) with a particle

size of approximately 50 nm as shown in scanning electron microscope (SEM) in Figure 2a (see a low magnified SEM image in Figure S1). Atransmission electron microscope (TEM) image and its fast Fourier transform (FFT) measurement exhibit that it has a high crystalline structure (with 0.31 nm d-spacing for (111) plane) which coincides with X-ray diffraction (XRD) patterns (Figure 2a,b). Then, a half-cell containing electrode with SiNPs-CNTs, Li_6PS_5Cl for a solid-state-electrolyte (SSE) separator, and Li foil were prepared for fabrication and evaluation of LiSi-C interlayer (see detailed preparation information in Method). The prepared cell (SUS/SiNPs-CNTs/SSE/Li) was charged in constant current mode until cut-off voltage of 5 mV (Figure 2d). A cross-sectioanl SEM images show that the SiNPs/CNTs layer with a thickness of 2 μm (Figure 2e,f) was transformed to the LiSi-C layer with a thickness of 3.25 μm after first charging (see Figure 2g and see the Figure. S2 for measurement of LiSi-C thickness). It is noticeable that the large-sized pores (> 1 μm) in SiNPs/CNTs were highly decreased to nanosized after electrochemical lithiation (Figure 2h). The decreased-sized pores allow Li to be deposited in small size inside LiSi-C layer. According to the previous works on behavior of inorganic material (Sn), diffusive processes mediating Coble diffusion softening which is one of the deformation mechanism is dominant at very small sample size[38]. The deformation of LiSi-C can be avoided by such small sized Li formation within such tiny pores during Li stripping process, which ensures the mechanical stability of both LiSi-C and SSE separator (more detailed is demonstrated in post-mortem analysis). To evaluate the role of stack pressure on the size of pores, we tested the cells under different stack pressure (5 Mpa and 64 Mpa is applied to cells as shown in Figure 2j and 2h, respectively). We observed that the less external stack pressure applied to cell, the more the pore size (can be assgined to gap between interparticles of LiSi) increase and the LiSi-C interlayer does not get dense (Figure 2j). In addition, as shown in Figure 2i, there is a small gap between LiSi-C and SUS current collector after disassembling solid-cell while LiSi-C and SSE remined fully attached. Such perfect attachment can be explained by Si volumetric expansion which introduces compressive stress to the SSE and ductile (soft) properties of LiSi and Li_6PS_5Cl. These result in relatively stronger adhesion between SSE and LiSi-C interlayer than interface between LiSi-C and SUS.

To find out the compatibility of SiNPs-CNTs (or LiSi-C) with Li_6PS_5Cl, X-ray diffraction (XRD) analysis of cells such as SUS/SSE/LiSi-C, SUS/SSE/SiNPs-CNTs, and SSE was conducted as shown in Figure S3. We observed that there were no changes in Li_6PS_5Cl crystalline structures when contacting between SiNPs-CNTs and SSE as well as even after the lithiation of SiNPs-CNTs layer. These results imply that Si and LiSi are thermodynamically and electrochemically stable against Li_6PS_5Cl and excessive amount of by products formation is limited kinetically. In addition, even though the peak assigned to the crystalline-Si disappeared after lithiation, we can see that the peak assigned to the crystalline-$Li_{3.75}Si$ in XRD analysis as shown in Figure S4 ($Li_{3.75}Si$ is fully lithiated state. For the formation of $Li_{22}Si_5$, much higher temperautre is required)[39-41].

Despite no electrolytes in the SiNPs-CNTs layer, SiNPs can be fully lithiated because 1) Li and Si alloying reaction accompanying volume expansion helps to offer Li-ion pathway by increasing the number of particle contact 2) lithiated Si itself has relatively higher ionic and electronic conductivity than pure Si. In the SUS/SSE/LiSi-C, we also can see the voltage plateau indicating delithiation of crystalline-$Li_{3.75}Si$ (Figure S5) which is commonly seen in LIBs[42,43]. Based on these results, interlayer thickness and material density of the $Li_{3.75}Si$ phase were obtained and we calculated the porosity of the SiNPs-CNTs (58.5%) and LiSi-C layer (11.0%) as shown in Figure 1k and Table. S1.

Behavior of Li deposition/stripping at LiSi-C interlayer. To verify the favorable effect of the LiSi-C interlayer on the ASSBs, electrochemical characterization was conducted with a half-cell (SUS/LiSi-C/SSE/Li) and it was compared without the LiSi-C interlayer (denoted to SUS/SSE/Li). After electrochemical lithiation of SiNPs/CNTs for LiSi-C (cut-off charge voltage: 0.005 V), it was further charged at a current density of 0.13 mA cm^{-2} for Li plating for 20 hours (areal capacity: 2.55 mAh cm^{-2}) and discharged at a current density of 0.25 mA cm^{-2} for Li stripping. The cut-off voltage of 200 mV was applied for Li stripping process for LiSi-C to avoid Si delithiation that potentially causes severe morphological change due to the volume shrinkage. At the beginning of Li deposition in a voltage profile at the first cycle, there were significant voltage dip and flat voltage plateau (Figure 3a) and Li metal nucleation overpotential can be calculated using the difference between the bottom of the voltage dip and voltage plateau. We confirmed that the nucleation overpotential of SUS/LiSi-C/SSE/Li and SUS/SSE/Li was calculated to 1.5 mV and 14.2 mV, respectively. Almost ten times lower nucleation overpotential in SUS/LiSi-C/SSE/Li arises from 1) intrinsic properties of LiSi with high lithiophilicity 2) high surface area of porous LiSi-C interlayer offering numerous Li nucleation sites (i.e. increased true contact area between SSE and current collector). On the other hand, the nucleation sites which are contact points (area) at the interface between SUS and SSE in SUS/SSE/Li are much less than the total nucleation sites derived from the porous MIEC LiSi-C interlayer and its interface (SUS and LiSi-C). So when the same current is applied to these cells, the actual current for Li deposition is much higher in SUS/SSE/Li configuration.

Notably, there were two voltage dips in SUS/LiSi-C/SSE/Li as shown in the inset of Figure 3a. To investigate these characteristics, we monitored LiSi-C interlayer by detaching SUS from it after lithiation of about 0.05 and 0.1 mAh cm^{-2}, which are roughly assigned to 3.1 and 3.7 mV. SEM images of LiSi-C lithiated with 0.05 mAh cm^{-2} exhibit a smooth surface (Figure S6), which implies that Li_{BCC} growth inside LiSi-C layer fills out the pores. In the case of 0.1 mAh cm^{-2}, LiSi-C is covered by black plates, expected that Li deposition occurs between LiSi-C layer and SUS (Figure S7). These phenomena of Li nucleation and growth between the LiSi-C and SUS result from not only the enhanced adhesion of the interface between LiSi-C and SSE but also the high Li conductive pathway of LiSi-C. XRD analysis shows that Li_2S derived from the decomposition of

Li_6PS_5Cl is clearly seen in SUS/SSE/Li after Li deposition (2.55 mAh cm^{-2}) while there are a few in SUS/LiSi-C/SSE/Li (Figure 3b), which implies that LiSi-C interlayer completely prevents direct contact between Li and SSE. Such stable Li deposition behaviors in SUS/LiSi-C/SSE/Li bring about high reversibility of Li transport during the charging and discharging process. Accordingly, when the capacity portion coming from the Si (0.68 mAh cm^{-2}) was subtracted, the SUS/LiSi-C/SSE/Li has initial Coulombic efficiency (CE) of 96.4% which is much higher than that of 89.4% in SUS/SSE/Li (Figure 3c).

To further prove above-mentioned phenomena, we investigated the Li morphology and location in each cell during the Li plating and stripping process. The cross-sectional SEM images and its corresponding energy-dispersive X-ray spectroscopy (EDX) for SUS/LiSi-C/SSE/Li show that the uniformly and densely deposited Li between LiSi-C and SUS current collector after plating (Figure 3d,f) and the LiSi-C interlayer preserves its original shape without any morphological changes (Figure 3e). After subsequent Li stripping, the Li disappears completely and the photograph of the electrode exhibits the clean surface of the SUS current collector (Figure 3g,h). On the other hand, SUS/SSE/Li shows deposited Li having a porous structure and some of the powder speculated as a SSE is embedded in the Li layer (Figure 3i,k). Moreover, there are regions where partially deposited Li, indicating that inhomogeneous Li deposition occurs. These can give rise to increase of the localized current density accompanying Li dendrite growth and difference of the local pressure in ASSBs (Figure 3j). More severely, after Li stripping, it is seen that some of the Li with random shape still exists on the current collector in both cross-sectional SEM images and the photograph (Figure 3l,m).

Identifying functions of components for LiSi-C interlayer. To further understand the role of the silicon and CNTs in the LiSi-C layer, we compared the SUS/LiSi-C/SSE/Li and other asymmetric cell configurations including the only CNTs (denoted to SUS/C/SSE/Li) and LiSi layer without CNTs (denoted to SUS/LiSi/SSE/Li). The SUS/C/SSE/Li showed a lower nucleation overpotential than that of SUS/SSE/Li because the high surface area of CNTs with many contact points with SSE offers numerous nucleation sites in the first cycle (Figure 4a). However, relatively low ionic conductivity in CNTs (compared to SSE) is likely to bring about the excessive Li plating on the top of the CNTs layer, and then Li directly contacting with SSE easily reacts with SSE and cause severe decomposition of the SSE as the case of the SUS/SSE/Li. The decomposition reactions concentrated at the Li clusters lead to stress concentration again and again and the formation of large cracks eventually brings about the cells to short-circuit[19-21]. On the other hand, we observed that SUS/LiSi/SSE/Li exhibits outstanding stability and cyclability without any short-circuiting for 80 hours (h) even at a higher current density of 0.30 and 0.92 $mAcm^{-2}$ (Figure 4b) compared to SUS/C/SSE/Li and SUS/SSE/Li. One of the reasons for such a high stability of the SUS/LiSi/SSE/Li owes for the electrochemical stability of the LiSi against SSE layer which was discussed earlier. Notably, adding CNTs to the LiSi interlayer was found to greatly improve the cycling time (> 250 h) and it also shows high Coulombic efficiency (99.3%,

average value for 35 cycles) and no capacity degradation as shown Figure 4c (see cycle life and its corresponding Coulombic efficiency of SUS/LiSi/SSE/Li in Figure S8). The results from comparing different cell configurations enlighten the role of CNT in improving the ASSB performance in combination with Si as most abundant element on the earth.

Specifically, homogenously distributed CNTs with high electron conductivity not only help the formation of uniform LiSi during electrochemical lithiation but also induce better plating and stripping of Li in LiSi-C compare to the cell without CNTs (SUS/LiSi/SSE/Li). In addition, CNTs act as binder during the electrode fabrication process of SiNPs-CNTs because of its magnificant mechanical peropertis (high modulus of about 1 TPa and high tensile strength of more than 10 GPa) and networking structure[44]. Since adhesion (between the SUS current collector and SiNPs) and interparticle contact between SiNPs without binder are poor, there might be some detachment accompanying holes in the electrode of SiNPs without CNTs. Such mechanical failure diminishes the functions of the interlayer even after the lithiation of the SiNPs electrode and Li deposition process. These result in the decomposition of Li_6PS_5Cl which contributes to low Coulombic efficiency and short-circuiting issues during cycles. In the ASSBs configuration, although polymer-based binders can be used, they could increase the interface resistance owing to their low electrical and ionic conductivity. Therefore, we emphasize that role of the CNTs as binder enhances the adhesion between the SUS and SiNPs-CNTs layer and contact of interparticle during the electrode fabrication process. Subsequently, the other role of these CNTs is to improve the mechanical strength of LiSi interlayer which can be fractured by compressive stress derived from the enormous thickness change of Li plating (~ 15 μm assinged to areal capacity of 3 mAh cm^{-2}). The addition of CNTs to SiNPs is like that of reinforced cement concrete in which relatively low tensile strength and ductility of concrete are compensated by steel bars having higher tensile strength and ductility. Such mechanically reinforced LiSi-C electrode preserving morphological integrity further strengthens its function as a protective interlayer. As proof of such assertions, under the harsh mechanical environment of stretched and bent LiSi-C electrode, the fact that CNTs seem to struggle to prevent the fracture of LiSi in the top-viewed SEM images was discovered (Figure S9). As a result, based on the electrochemical results (performance of CNTs, LiSi, and LiSi-C layer in asymmetric cell), we confirmed that the electrochemical performance of LiSi can be further enhanced by adding the CNTs.

Practical feasibility of LiSi-C interlayer. To verify the practical feasibility of LiSi-C interlayer, a full-cell containing cathodes needs to be evaluated in this ASSBs configuration because of the unstable interface between the Li_6PS_5Cl and Li foil in a half-cell. Moreover, when considering the properties of our LiSi-C interlayer where an additional Li source is always required for electrochemical lithiation of SiNPs before operating a cell, it is necessary for the full-cell to include an additional amount of cathode. However, such an extra amount of cathode materials only used for the formation of LiSi-C brings about the decreased

volumetric/specific energy density and raised resistance in the aspect of cell design (e.g. high areal capacity of the electrode could result in high cell resistance) because of its thicker electrode. Having noticed that the Si functions as a lithiophilic material promoting good wetting property with liquefied Li[45], we considered non-electrochemical lithiation in which Si physically contacting with Li could be lithiated and transformed to LiSi without any current to avoid the use of extra cathode loading in a full-cell. To confirm that solid-state Li-metal also can give rise to smooth lithiation of micron-scaled SiNPs/CNTs layer as liquefied Li, *in-situ* SEM analysis was conducted using a single micron-sized Si particle (Figure 4d). We monitored that the Si particle was lithiated for a few seconds, expanded, and fractured, which are commonly observed in Si anode material during electrochemical lithiation. Based on this experimental work, we adopted an approach to fabricate a full-cell with thin Li-metal foil (~ 30 μm shown in Figure S10) located between the current collector and SiNPs/CNTs layer. The full-cell with NCM811 cathode (denoted to Li/Si-C/SSE/NCM811) was investigated and the cross-sectional SEM images and its corresponding EDX (Figure 4e) confirmed that SiNPs/CNTs layer was transformed to LiSi-C layer without any current. The magnified image in Figure 4f shows a highly densified LiSi-C layer similar to what exhibited in electrochemical lithiation of the half-cell of SUS/LiSi/SSE/Li. In addition, the voltage region assigned to the alloying reaction of Si with Li is not seen in the voltage profile of a symmetric cell (Li/SSE/SiNPs-CNTs/Li) as shown in Figure 4g, which also indicates that SiNPs-CNTs can be lithiated by contacting with Li without current.

Electrochemical characterization of the prepared full-cell (Li/Si-C/SSE/NCM811) was conducted and a full-cell of Li/SSE/NCM811 was also fabricated to substantiate the effectiveness of LiSi-C layer in ASSBs for comparison. The cells were examined over the range 2.8-4.3 V at 0.1C for the first cycle and 0.35C for the rest of the cycles (the detailed cell preparation and electrochemical measurements are provided in the Method). The voltage profile exhibits that the initial specific capacity of cathode materials in each cell (207.8 mAh g^{-1} for Li/Si-C/SSE/NCM811 and 205.1 mAh g^{-1} for Li/SSE/NCM811) was similar (Figure 5a). The initial CE of Li/Si-C/SSE/NCM811 is 92.0% higher than that (86.5%) of Li/SSE/NCM811 (Figure 5b). This result indicates that LiSi-C pre-formed by contacting the Li foil also prevents direct contact between Li and SSE as well as chemical reduction of Li_6PS_5Cl, which coincides with the result of the half-cell. More interestingly, the de-alloying reaction of LiSi (assigned to a range of 3.2-3.4 V) is not shown in the voltage profile during discharging to a cut-off voltage of 2.8 V. This is because Li foil used for lithiation of SiNPs-CNTs supplies enough source of Li to the cathode and the stripping overpotential of LiSi is higher than that of Li, and therefore LiSi-C layer here functions as not active material but Li-ion pathway. Without any Li source in a cell configuration of Si-C/SSE/NCM811, we can see the de-lithiation of LiSi upon discharging process (Figure S11).

In the cycling test of full-cell, Li/Si-C/SSE/NCM811 shows capacity retention of 94.6% after 100 cycles and

88.9% after 200 cycles, and its CE reaches 99.9% after tens of cycles. On the other hand, the drastic capacity fading started occurring after 30 cycles in the full-cell without LiSi-C interlayer (Li/SSE/NCM811). As shown in Figure S12a, the cell (Li/SSE/NCM811) under a much higher stack pressure of 64 Mpa showed a sudden capacity drop due to short-circuiting, implying that the mechanism of cell degradation differs depending on the stack pressure in the case of without LiSi-C layer. These results are expected that 1) growth of Li dendrites through non-protected SSE reaches cathode (battery short-circuiting) 2) the soft property of Li metal and environment of the highly compressed cell allows Li to extruded through the SSE. However, the cell containing LiSi-C layer shows outstanding electrochemical performance regardless of stack pressure (voltage profiles of Li/Si-C/SSE/NCM811 at stack pressure of 5 Mpa is shown in Figure S12b for comparison with Li/SSE/NCM811). These results indicate that LiSi-C interlayer enables the ASSBs systems to be operating without high stack pressure which has been considered as a one of obstacles for practical application.

In addition, the rate capability of the full-cell with LiSi-C interlayer was studied by varying the discharge rate from 0.05C to 5C at a fixed charge rate of 0.05C in a constant current mode and we observed that the discharge capacity was about 82.8% at 2C and 76% at 5C compared to the original capacity at 0.05C (Figure 5c,d). Furthermore, discharge capacity and cyclability at low temperature were investigated as a crucial parameter affecting the electrochemical performance and as a critical decision point for battery application in electric vehicles (EVs) industry. As the temperature decreased to 20 °C, the areal capacity of the Li/Si-C/SSE/NCM811 was 2.4 mAh cm^{-2} which is 85.8% capacity retention comparable to that attained at 60 °C (Figure 5e). The capacity was sustained without a significant decrease and remained at 97.65% after 49 cycles (Figure 5f).

Post-mortem analysis using each full-cell (after 200 and 73 cycles for Li/Si-C/SSE/NCM811 and Li/SSE/NCM811, respectively) with the discharged state was conducted in terms of morphological change of Li metal, LiSi-C layer, and their interfaces. As clearly shown in Figure 6a,b, the LiSi-C layer not only separates the SSE and Li clearly but also preserves its morphological integrity without any spallation or deformation for the Li/Si-C/SSE/NCM811. In order to cause morphological change of LiSi with a high modulus (Young's modulus: 41 Gpa and hardness: 1.9 Gpa), Li_{BCC} nucleated in LiSi needs to afford the stress[46,47]. However, such stress of LiSi is much higher than the hardness (~7 – 43 Mpa) and yield strength (0.6 – 1.3 MPa) of Li_{BCC}[48], therefore the creep of Li located inside LiSi is inevitable during the lithiation, which leads to preserving morphology of LiSi. In addition, the reinforced mechanical strength of LiSi-C by adding CNTs as well as the minimized hardness of Li_{BCC} derived from its size effect described in Figure 2j further help to avoid deformation of LiSi-C interlayer. Furthermore, there is densified Li with a smooth surface even after 200 cycles because of outstanding properties of LiSi-C layer as an interlayer (Figure S13a), which coincides with reversible Li plating/stripping phenomena described in Figure 3. In the case of the Li/SSE/NCM81, there

seems porous structure at the boundary between the SSE and Li and Li also has the feature of porous and mossy like structure that might come from the dendritic Li formation and inhomogeneous striping upon repeated cycling (Figure 6c,d Magnified cross-sectional SEM images of Li side is shown in Figure S13b).

Conclusion

In summary, we showed an ultra-thin LiSi-C MIEC interlayer (3.25 μm) with features of porous structure as a part of ASSBs using a Li_6PS_5Cl separator. In the asymmetric cell of SUS/LiSi-C/SSE/Li (electrochemical lithiation process), we observed that dense metallic Li can form and grow out between the current collector and LiSi-C interlayer, and the formation of by-products originating from the decomposition of SSE was highly limited. Without this MIEC interlayer, inhomogeneous Li deposition and formation of unwanted residues such as Li_2S occurs during plating/stripping, which leads to poor Coulombic efficiency. For the full-cell, we used a Li foil (30 μm) directly contacting with SiNPs-CNTs (i.e. non-electrochemical lithiation) to prevent consumption of Li source in the NCM811 cathode. A full-cell (Li/Si-C/SSE/NCM811) demonstrated stable cycling stability of 88.9% after 200 cycles and 97.65% after 49 cycles at 60 and 20 °C, respectively. On the other hand, drastic capacity fading was seen in Li/SSE/NCM811. As a result, we highlight that the exquisitely designed ultra-thin LiSi-C MIEC interlayer paves the path for commercially feasible ASSBs with both high-energy density and safety, thus bringing about the realization of EVs with more extended driving mileage.

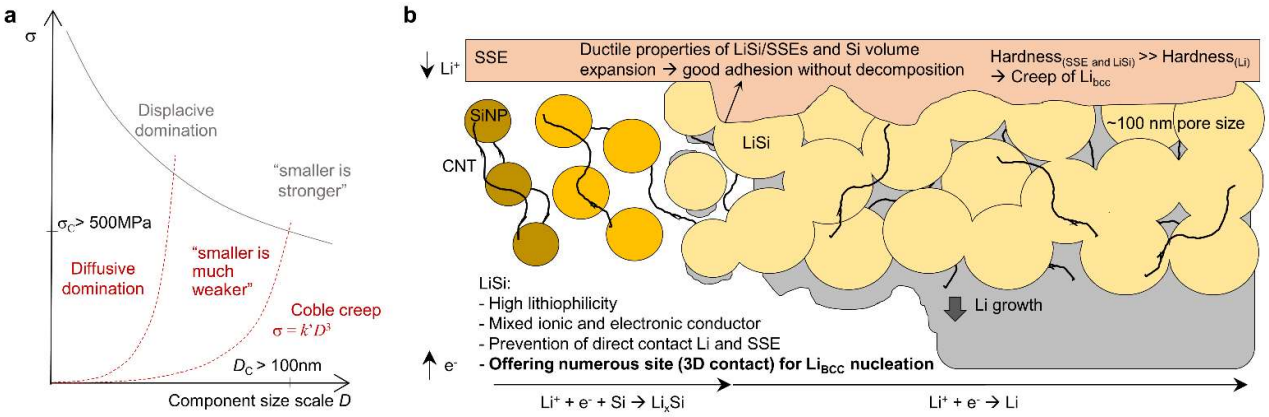

Figure 1 | Li_{BCC} deposition mechanisms at LiSi-C interlayer in ASSBs. a, Semi-quantitative illustration of deformation mechanism map for Sn. Grey curve denotes displacive deformation (Hall-Petch strengthening predicts"smaller is stronger" trend). Surface diffusional deformation is governed by Coble creep. At a fixed strain rate, it shows "smaller is weaker" (Red curve). **b**, Schematic illustration (cross-section) of LiSi-C interlayer in terms of Li_{BCC} deposition mechanism. Increase of state of charge (alloying reaction of Si, $xLi^+ + e^- + Si \rightarrow Li_xSi$ and Li deposition, $Li^+ + e^- \rightarrow Li$) is shown to the right direction.

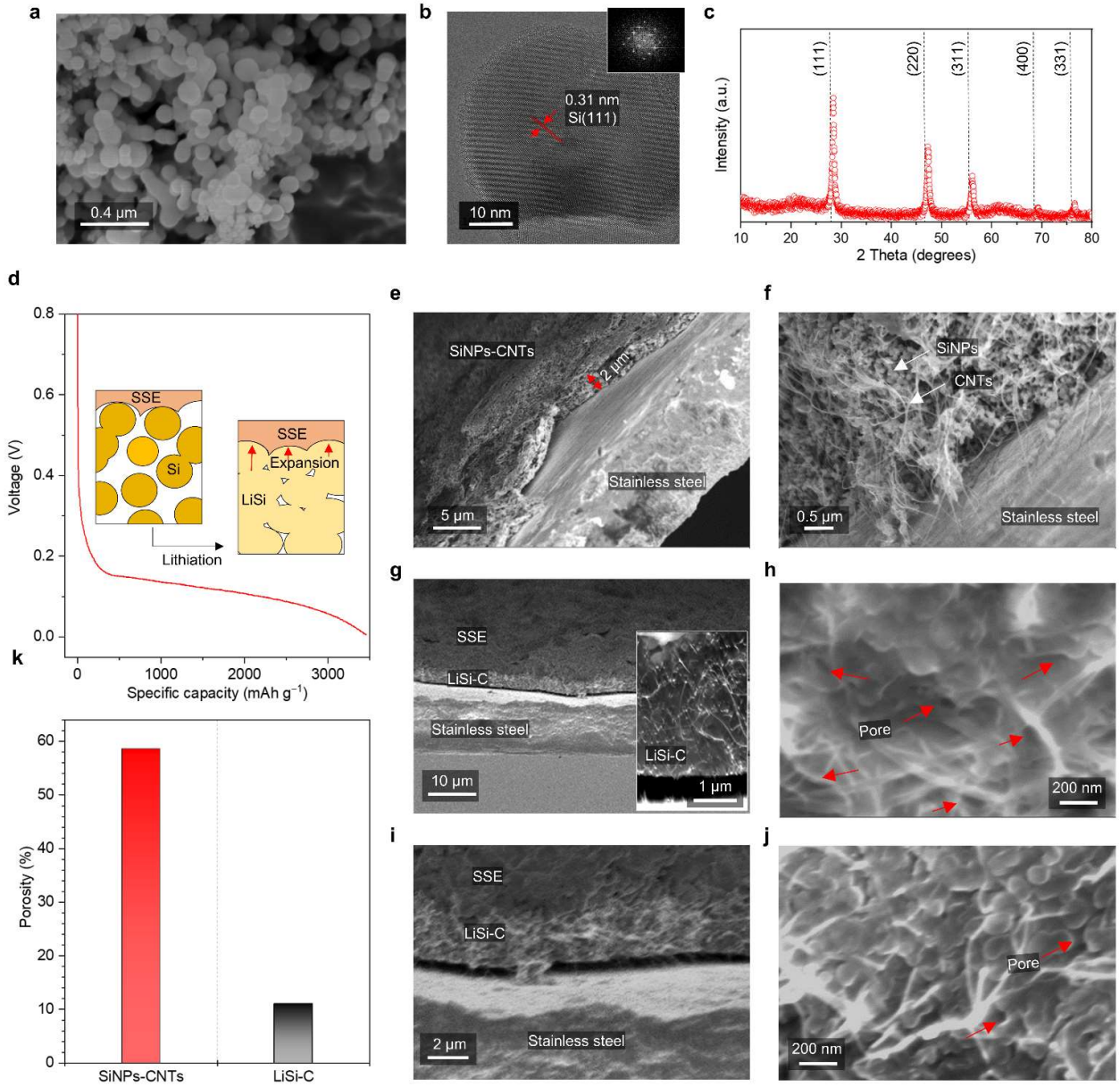

Figure 2 | Electrochemical lithiation for fabrication of LiSi-C interlayer. a, SEM images of SiNPs with the particle size of 50 nm. **b**, TEM images of single Si particle with d-spacing of 0.31 nm and inset showing a *Fast Fourier Transform*. **c**, XRD analysis of SiNPs. **d**, Voltage profile of SiNPs-CNTs electrode in ASSBs with an inset indicating the morphological change during lithiation. **e**,**f**, Cross-sectional SEM images of SiNPs-CNTs. **g**, Cross-sectional SEM image of LiSi-C layer with an inset showing magnified image. This layer was obtained after charging process of SiNPs-CNTs at cut-off voltage of 0.005 V under stack pressure of 65 Mpa. **h**, Top-viewed SEM images of LiSi-C layer (red arrow indicates the pores). **i**, Cross-sectional SEM image of LiSi-C layer. **j**, Top-viewed SEM images of LiSi-C layer produced under stack pressure of 5 Mpa (red arrow indicates the pores). **k**, The porosity of SiNPs-CNTs (58.5%) and LiSi-C layer (11.0%) is calculated based on

the thickness and density of each layer.

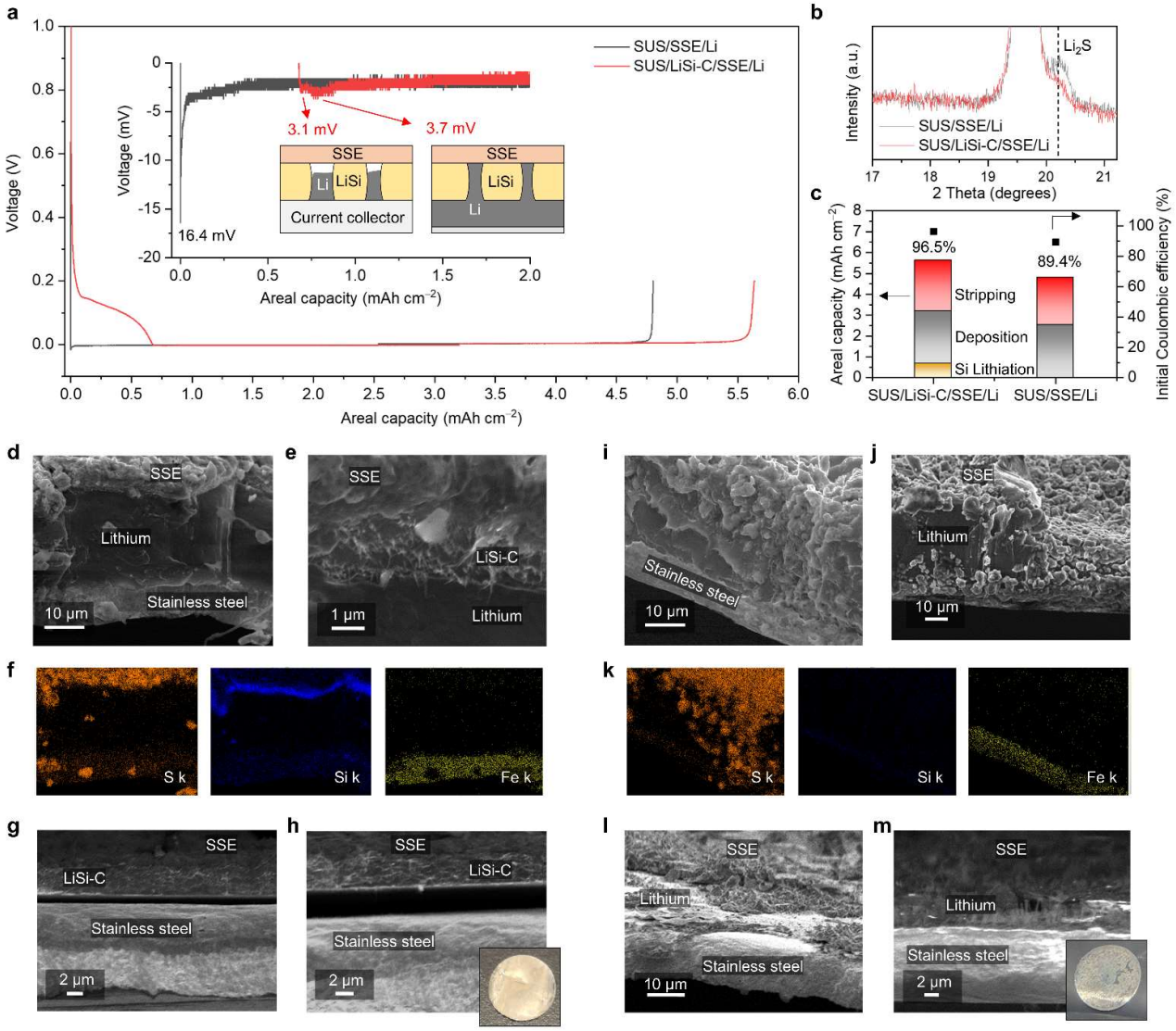

Figure 3 | Investigation of interface depending on existance of LiSi-C. a, Voltage profiles of half-cells (SUS/LiSi-C/SSE/Li and SUS/SSE/Li) at the first cycle. The insets show magnified voltage profile indicating overpotential of each cell and schematic illustration exhibiting behavior of Li deposition process in the LiSI-C layer located between SSE and current collector. **b**, XRD analysis (Mo Kα of wavelength 0.7107 Å) of SSE surface contacting with LiSi-C and SUS in SUS/LiSi-C/SSE/Li and SUS/SSE/Li, respectively, after Li deposition process. **c**, Bar graph assigned to each Si lithiation, Li deposition, and stripping shows areal capacity and initial Coulombic efficiencies. **d-h**, Cross-sectional SEM images of SUS/LiSi-C/SSE/Li after Li deposition (**d,e**) and its corresponding EDS mapping (**f**) as well as after Li stripping (**g**,**h**) with an inset of photograph of stainless steel current collector detached from SSE. **i-m**, Cross-sectional SEM images of SUS/SSE/Li after Li deposition (**i,j**) and its corresponding EDS mapping (**k**) as well as after Li stripping (**l**,**m**) with an inset of photograph of stainless steel current collector detached from SSE.

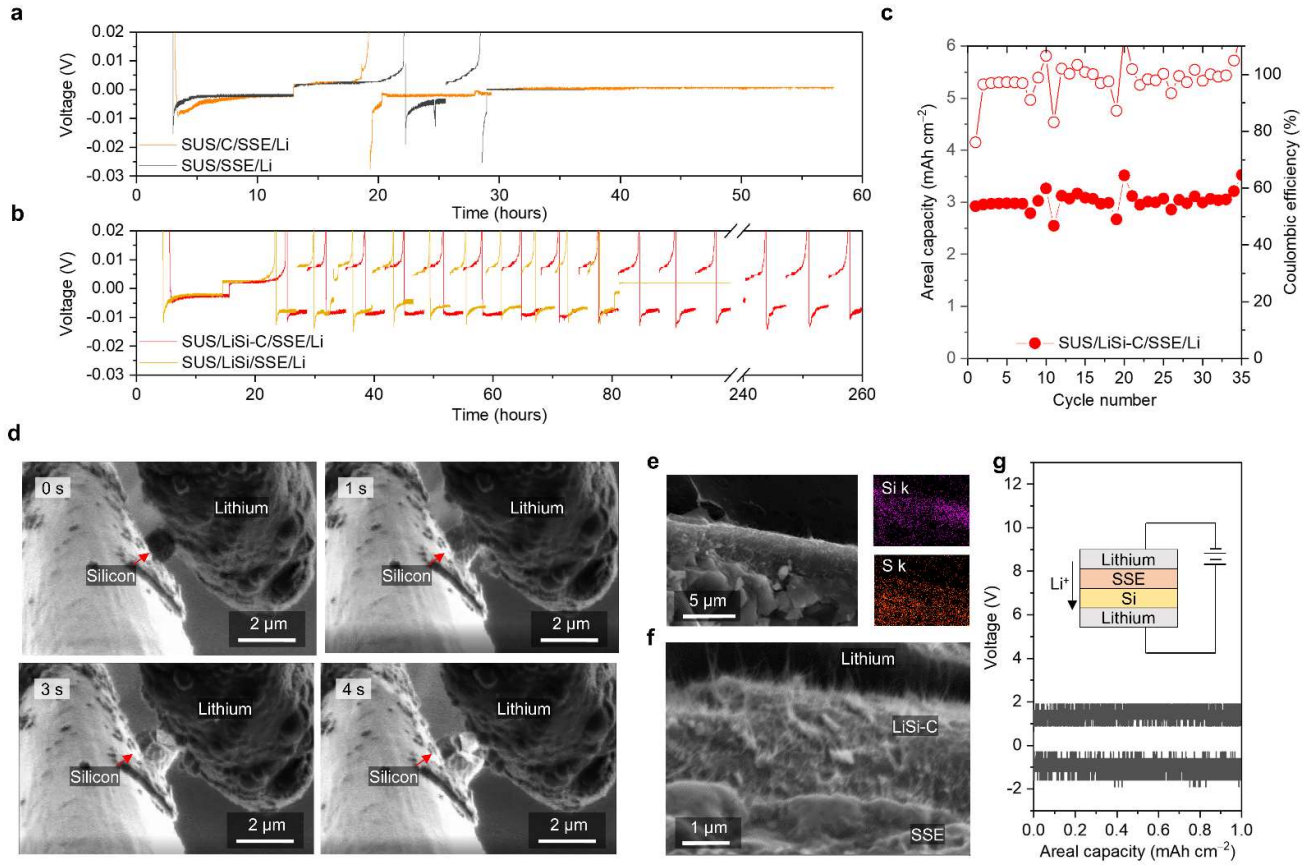

Figure 4 | Electrochemical characterization of various interlayer. a, The comparison of cyclic performance between SUS/C/SSE/Li and SUS/SSE/Li (half-cell, asymmetric cells) at current density of 0.1 and 0.3 mA cm^{-2} of first (10 h) and rest of cycles (3.3 h), respectively (areal capacity: 1.0 mAh cm^{-2}). **b**, The comparison of cyclic performance between SUS/LiSi-C/SSE/Li and SUS/LiSi/SSE/Li at current density of 0.3 and 0.92 mA cm^{-2} of first (10 h) and rest of cycles (3.3 h), respectively (areal capacity: 3.0 mAh cm^{-2}). **c**, Areal capacity retention and Coulombic efficiency of SUS/LiSi-C/SSE/Li in a half-cell. **d**, Observation of phenomenon when silicon single particle contacts with Li clusters (non-electrochemical lithiation) through the *in-situ* SEM images. **e**, Cross-sectional SEM image and its corresponding EDS mapping images of non-electrochemically lithiated SiNPs-CNTs electrode (non-electrochemical lithiation means physical contact of LiSi-C and Li foil). **f**, Magnified cross-sectional SEM images of LiSi-C interlayer. **g**, Voltage profile of symmetric cell (Li/SSE/Si/Li) with an inset showing its circuit diagram.

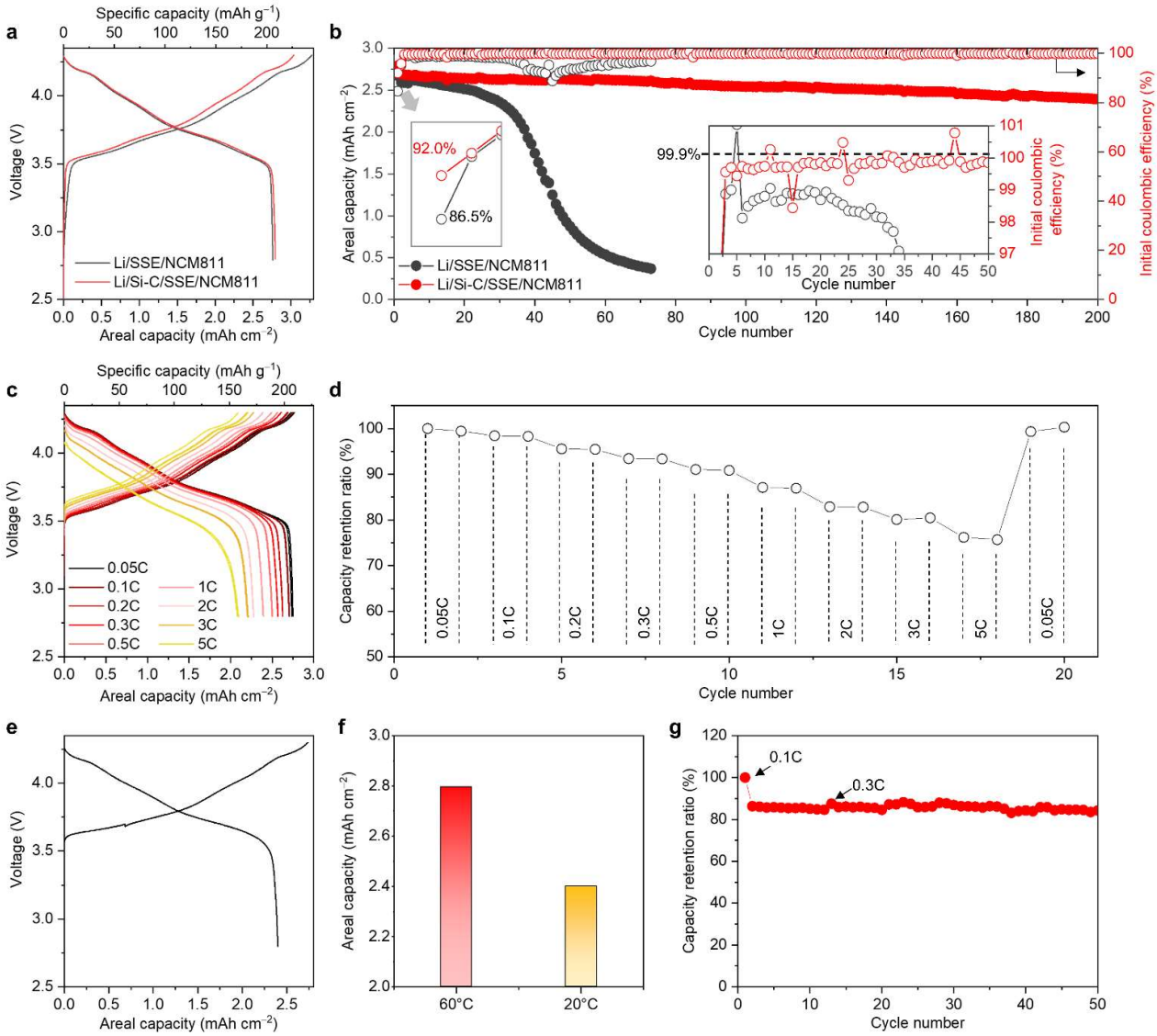

Figure 5 | Electrochemical characterization (full-cell) of LiSi-C interlayer. a, Charge and discharge profile of Li/SSE/NCM811 and Li/Si-C/SSE/NCM811 at the first cycle at stack pressure of 35 and 64 Mpa, respectively. **b**, Areal capacity retention and Coulombic efficiency of each cell at operating temperature of 60 °C. Insets exhibiting the magnified graph of (initial) Coulombic efficiency for the first cycle and 50th cycles. **c**,**d**, Voltage profile (**c**) and capacity retention ratio (**d**) of Li/Si-C/SSE/NCM811 at different rate of 0.05C – 5C. **e**, Voltage profiles of Li/Si-C/SSE/NCM811 at 20 °C. **f**, Comparison of areal capacity of Li/Si-C/SSE/NCM811 at different operating temperature of 60 and 20 °C. **g**, Capacity retention ratio of Li/Si-C/SSE/NCM811 at 20 °C.

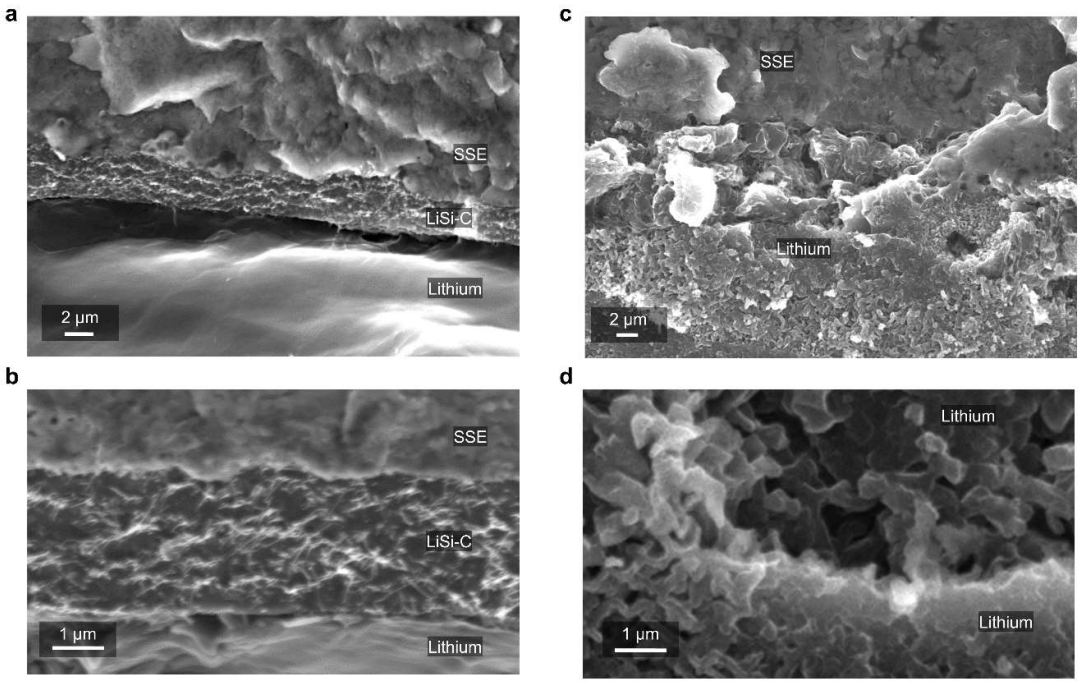

Figure 6 | Post-mortem analysis of LiSi-C interlayer. a,b, Cross-sectional SEM images of Li/Si-C/SSE/NCM811 after 200 cycles. **c.d**, Cross-sectional SEM images of Li/SSE/NCM811 after 73 cycles.

Methods

Electrode preparation. The SiNPs-CNTs electrode was fabricated using commercial SiNPs (Alfa Aesar), CNTs (Tuball), and DI-water solvent (the mass ratio of SiNPs : CNTs was 90:10). The dispersion solution was mixed and stirred vigorously in a planetary centrifugal mixer (Thinky Corporation, AR-100) and it was cast on the SUS foil (thickness is ~ 0.01 mm) up to 0.21 mg cm^{-2}. The electrode was then dried at 110 °C for 6 h in the vacuum oven. The other electrodes (SiNPs and CNTs) were fabricated at the same condition above-described.

Cell preparation. All ASSBs in this study was fabricated using pellet cell (Canrd, China). For the half-cell, 90 mg power-typed Li_6PS_5Cl (NEI Corporation, United states) was loaded in a pellet cell (diameter of 1 cm) then was pressed at the pressure of 200 MPa. The prepared SiNPs-CNTs electrode and Li_6PS_5Cl separator layer were stacked together and they were pressed together at 700 MPa. After that, the Li foil with a thickness of 0.350 mm (XIAMEN TOB new energy technology Co., LTD.) was put on the other side of SiNPs-CNTs electrode. For the full-cell, niobium coated NCM811, Li_6PS_5Cl, and carbon black (Super P, TIMCAL) were first mixed in a mortar at the weight ratio of 67 : 30 : 3, respectively. The prepared cathode mixture (20 mg cm^{-2}), Li_6PS_5Cl, and SiNPs-CNTs electrode were stacked together in this order and pressed at 700 MPa. Then, the Li foil (30 μm) were added to the bottom of the SiNPs-CNTs electrode. As sulfide-based materials and Li are sensitive to air and moisture, all these procedures were done within an Argon-filled glovebox (H_2O < 1.0 ppm, O_2 < 1.0 ppm).

Electrochemical characterization. For electrochemical lithiation of SiNPs-CNTs electrode, a constant current of 0.3 mA cm^{-2} (0.45C) was applied until cut-off voltage of 0.005 V. The electrochemical assessment (Li plating/stripping process) was carried out in the half-cell. For the SUS/SSE/Li and SUS/C/SSE/Li, the constant current of 0.1 mA cm^{-2} was applied for 10 h for charging and it was discharged a current of 0.1 mA cm^{-2} until the cut-off voltage of 0.2 V at the first cycle. The constant current of 0.3 mA cm^{-2} was applied for 3.3 h for charging and it was discharged a current of 0.3 mA cm^{-2} until the cut-off voltage of 0.2 V for the rest of cycles. The areal capacity was about 1.0 mAh cm^{-2}. For the SUS/LiSi/SSE/Li and SUS/LiSi-C/SSE/Li, the constant current of 0.3 mA cm^{-2} was applied for 10 h for charging and it was discharged a current of 0.3 mA cm^{-2} until the cut-off voltage of 0.2 V at the first cycle. The constant current of 0.92 mA cm^{-2} was applied for 3.3 h for charging and it was discharged a current of 0.92 mA cm^{-2} until the cut-off voltage of 0.2 V for the rest of cycles. The areal capacity was about 3.0 mAh cm^{-2}. The electrochemical assessment was conducted in the full-cell in a voltage range of from 2.8 to 4.3 V at a rate of 0.1 C (constant current of 0.28 mA cm^{-2}) for the first cycle and 0.35 C (constant current of 0.98 mA cm^{-2}) for the rest of the cycles. Electrochemical analysis of all half-cells and full-cells was conducted using a battery cycler (Neware).

Material characterization. Morphological investigation for the materials, electrode, and cells was conducted using SEM and EDS (Zeiss Merlin) and high-resolution TEM (JEM-2100F, JEOL). The two X-ray diffractometers (AERIS, Malvern PANalytical with Cu Kα of wavelength 1.542 Å and Empyrean, Malvern PANalytical Mo Kα of wavelength 0.7107 Å) were used for the physicochemical characterization. To examine the morphological change of samples after cycles, the cycled cells were disassembled in an Ar-filled glove box (H_2O < 1 ppm, O_2 < 1 ppm) and then the electrode was cut by scissors for analysis of cross-sectional SEM images. For the observation of micron-sized silicon lithiation (i.e. non-electrochemical lithiation as mentioned in Results and Discussion), *in-situ* technique was conducted using SEM (Verios 460, FEI).

Acknowledgements

This work is supported by by NSF CBET-2034902 and Honda Research Institute USA, Inc.

References

1 Li, W., Erickson, E. M. & Manthiram, A. High-nickel layered oxide cathodes for lithium-based automotive batteries. *Nature Energy* **5**, 26-34, doi:10.1038/s41560-019-0513-0 (2020).

2 Lu, J. *et al.* The role of nanotechnology in the development of battery materials for electric vehicles. *Nat Nano* **11**, 1031-1038 (2016).

3 Fotouhi, A., Auger, D. J., Propp, K., Longo, S. & Wild, M. A review on electric vehicle battery modelling: From Lithium-ion toward Lithium–Sulphur. *Renewable and Sustainable Energy Reviews* **56**, 1008-1021 (2016).

4 Niu, C. *et al.* High-energy lithium metal pouch cells with limited anode swelling and long stable cycles. *Nature Energy*, doi:10.1038/s41560-019-0390-6 (2019).

5 Liu, J. *et al.* Pathways for practical high-energy long-cycling lithium metal batteries. *Nature Energy*, doi:10.1038/s41560-019-0338-x (2019).

6 Yan, K. *et al.* Selective deposition and stable encapsulation of lithium through heterogeneous seeded growth. *Nature Energy* **1**, doi:10.1038/nenergy.2016.10 (2016).

7 Xu, R. *et al.* Artificial Interphases for Highly Stable Lithium Metal Anode. *Matter* **1**, 317-344, doi:10.1016/j.matt.2019.05.016 (2019).

8 Lin, D., Liu, Y. & Cui, Y. Reviving the lithium metal anode for high-energy batteries. *Nat Nanotechnol* **12**, 194-206, doi:10.1038/nnano.2017.16 (2017).

9 Gond, R., van Ekeren, W., Mogensen, R., Naylor, A. J. & Younesi, R. Non-flammable liquid electrolytes for safe batteries. *Mater Horiz* **8**, 2913-2928, doi:10.1039/d1mh00748c (2021).

10 Deng, K. *et al.* Nonflammable organic electrolytes for high-safety lithium-ion batteries. *Energy*

Storage Materials **32**, 425-447, doi:10.1016/j.ensm.2020.07.018 (2020).

11 Seino, Y. *et al.* Synthesis of phosphorous sulfide solid electrolyte and all-solid-state lithium batteries with graphite electrode. *Solid State Ionics* **176**, 2389-2393, doi:10.1016/j.ssi.2005.03.026 (2005).

12 Monroe, C. & Newman, J. The Impact of Elastic Deformation on Deposition Kinetics at Lithium/Polymer Interfaces. *Journal of The Electrochemical Society* **152**, doi:10.1149/1.1850854 (2005).

13 Sato, T. *et al.* Novel solid-state polymer electrolyte of colloidal crystal decorated with ionic-liquid polymer brush. *Adv Mater* **23**, 4868-4872, doi:10.1002/adma.201101983 (2011).

14 Baba, M. *et al.* Multi-layered Li-ion rechargeable batteries for a high-voltage and high-current solid-state power source. *Journal of Power Sources* **119-121**, 914-917, doi:10.1016/s0378-7753(03)00223-4 (2003).

15 Wan, J. *et al.* Ultrathin, flexible, solid polymer composite electrolyte enabled with aligned nanoporous host for lithium batteries. *Nat Nanotechnol* **14**, 705-711, doi:10.1038/s41565-019-0465-3 (2019).

16 Xu, L. *et al.* Toward the Scale-Up of Solid-State Lithium Metal Batteries: The Gaps between Lab-Level Cells and Practical Large-Format Batteries. *Advanced Energy Materials* **11**, doi:10.1002/aenm.202002360 (2020).

17 Tan, D. H. S., Banerjee, A., Chen, Z. & Meng, Y. S. From nanoscale interface characterization to sustainable energy storage using all-solid-state batteries. *Nat Nanotechnol* **15**, 170-180, doi:10.1038/s41565-020-0657-x (2020).

18 Tan, D. H. S. *et al.* Enabling Thin and Flexible Solid-State Composite Electrolytes by the Scalable Solution Process. *ACS Applied Energy Materials* **2**, 6542-6550, doi:10.1021/acsaem.9b01111 (2019).

19 Otoyama, M. *et al.* Visualization and Control of Chemically Induced Crack Formation in All-Solid-State Lithium-Metal Batteries with Sulfide Electrolyte. *ACS Appl Mater Interfaces* **13**, 5000-5007, doi:10.1021/acsami.0c18314 (2021).

20 Byeon, Y.-W. & Kim, H. Review on Interface and Interphase Issues in Sulfide Solid-State Electrolytes for All-Solid-State Li-Metal Batteries. *Electrochem* **2**, 452-471, doi:10.3390/electrochem2030030 (2021).

21 Schwietert, T. K. *et al.* Clarifying the relationship between redox activity and electrochemical stability in solid electrolytes. *Nature Materials* **19**, 428-435, doi:10.1038/s41563-019-0576-0 (2020).

22 Zhang, J. *et al.* Poly(ethylene oxide) reinforced Li6PS5Cl composite solid electrolyte for all-solid-state lithium battery: Enhanced electrochemical performance, mechanical property and interfacial stability. *Journal of Power Sources* **412**, 78-85, doi:10.1016/j.jpowsour.2018.11.036 (2019).

23 Choi, H. J. *et al.* In Situ Formed Ag-Li Intermetallic Layer for Stable Cycling of All-Solid-State Lithium Batteries. *Adv Sci (Weinh)* **9**, e2103826, doi:10.1002/advs.202103826 (2022).

24 Santhosha, A. L., Medenbach, L., Buchheim, J. R. & Adelhelm, P. The Indium−Lithium Electrode in Solid-State Lithium-Ion Batteries: Phase Formation, Redox Potentials, and Interface Stability. *Batteries & Supercaps* **2**, 524-529, doi:10.1002/batt.201800149 (2019).

25 Park, S. W. *et al.* Graphitic Hollow Nanocarbon as a Promising Conducting Agent for Solid-State Lithium Batteries. *Small* **15**, e1900235, doi:10.1002/smll.201900235 (2019).

26 Ye, L. & Li, X. A dynamic stability design strategy for lithium metal solid state batteries. *Nature* **593**, 218-222, doi:10.1038/s41586-021-03486-3 (2021).

27 Suzuki, N. *et al.* Highly Cyclable All-Solid-State Battery with Deposition-Type Lithium Metal Anode Based on Thin Carbon Black Layer. *Advanced Energy and Sustainability Research*, doi:10.1002/aesr.202100066 (2021).

28 Su, Y. *et al.* A more stable lithium anode by mechanical constriction for solid state batteries. *Energy & Environmental Science* **13**, 908-916, doi:10.1039/c9ee04007b (2020).

29 Simon, F. J., Hanauer, M., Richter, F. H. & Janek, J. Interphase Formation of PEO20:LiTFSI-Li6PS5Cl Composite Electrolytes with Lithium Metal. *ACS Appl Mater Interfaces* **12**, 11713-11723, doi:10.1021/acsami.9b22968 (2020).

30 Lee, Y.-G. *et al.* High-energy long-cycling all-solid-state lithium metal batteries enabled by silver–carbon composite anodes. *Nature Energy* **5**, 299-308, doi:10.1038/s41560-020-0575-z (2020).

31 Simon, F. J., Hanauer, M., Henss, A., Richter, F. H. & Janek, J. Properties of the Interphase Formed between Argyrodite-Type Li6PS5Cl and Polymer-Based PEO10:LiTFSI. *ACS Appl Mater Interfaces* **11**, 42186-42196, doi:10.1021/acsami.9b14506 (2019).

32 Pan, Q., Smith, D. M., Qi, H., Wang, S. & Li, C. Y. Hybrid electrolytes with controlled network structures for lithium metal batteries. *Adv Mater* **27**, 5995-6001, doi:10.1002/adma.201502059 (2015).

33 Mukherjee, R. *et al.* Defect-induced plating of lithium metal within porous graphene networks. *Nat Commun* **5**, 3710, doi:10.1038/ncomms4710 (2014).

34 Kim, S. Y. & Li, J. Porous Mixed Ionic Electronic Conductor Interlayers for Solid-State Batteries. *Energy Material Advances* **2021**, 1-15, doi:10.34133/2021/1519569 (2021).

35 Chen, Y. *et al.* Li metal deposition and stripping in a solid-state battery via Coble creep. *Nature* **578**, 251-255, doi:10.1038/s41586-020-1972-y (2020).

36 Zhu, T. & Li, J. Ultra-strength materials. *Progress in Materials Science* **55**, 710-757 (2010).

37 Frost, H. J. & Ashby, M. F. *Deformation mechanism maps: the plasticity and creep of metals and ceramics*. (Pergamon press, 1982).

38 Tian, L., Li, J., Sun, J., Ma, E. & Shan, Z. W. Visualizing size-dependent deformation mechanism transition in Sn. *Sci Rep* **3**, 2113, doi:10.1038/srep02113 (2013).

39 Sung, J. *et al.* Subnano-sized silicon anode via crystal growth inhibition mechanism and its application

in a prototype battery pack. *Nature Energy* **6**, 1164-1175, doi:10.1038/s41560-021-00945-z (2021).

40 Park, S. *et al.* Scalable Synthesis of Hollow β-SiC/Si Anodes via Selective Thermal Oxidation for Lithium-Ion Batteries. *ACS Nano* **14**, 11548-11557, doi:10.1021/acsnano.0c04013 (2020).

41 Sung, J. *et al.* Fabrication of Lamellar Nanosphere Structure for Effective Stress-Management in Large-Volume-Variation Anodes of High-Energy Lithium-Ion Batteries. *Adv Mater*, e1900970, doi:10.1002/adma.201900970 (2019).

42 Ma, J. *et al.* Strategic Pore Architecture for Accommodating Volume Change from High Si Content in Lithium-Ion Battery Anodes. *Advanced Energy Materials* **10**, 1903400, doi:10.1002/aenm.201903400 (2020).

43 Ma, J. *et al.* Towards maximized volumetric capacity via pore-coordinated design for large-volume-change lithium-ion battery anodes. *Nature Communications* **10**, doi:10.1038/s41467-018-08233-3 (2019).

44 Esawi, A. M. K. & Farag, M. M. Carbon nanotube reinforced composites: Potential and current challenges. *Materials & Design* **28**, 2394-2401, doi:10.1016/j.matdes.2006.09.022 (2007).

45 Liang, Z. *et al.* Composite lithium metal anode by melt infusion of lithium into a 3D conducting scaffold with lithiophilic coating. *Proceedings of the National Academy of Sciences* **113**, 2862-2867 (2016).

46 Qi, Y., Hector, L. G., James, C. & Kim, K. J. Lithium concentration dependent elastic properties of battery electrode materials from first principles calculations. *Journal of The Electrochemical Society* **161**, F3010 (2014).

47 Li, K. *et al.* From chemistry to mechanics: bulk modulus evolution of Li–Si and Li–Sn alloys via the metallic electronegativity scale. *Physical Chemistry Chemical Physics* **15**, 17658-17663 (2013).

48 Fincher, C. D., Ojeda, D., Zhang, Y., Pharr, G. M. & Pharr, M. Mechanical properties of metallic lithium: from nano to bulk scales. *Acta Materialia* **186**, 215-222, doi:10.1016/j.actamat.2019.12.036 (2020).

Supplementary information

Mixed Ionic and Electronic Conducting Ultra-Thin Lithium Silicide Interlayer for Solid-State Lithium Batteries

Jaekyung Sung[1,2], So Yeon Kim[1,2], Avetik Harutyunyan[3], Maedeh Amirmaleki[1,2], Sookyung Jeong[4], Yoonkwang Lee[5], Yeonguk Son[6], Ju Li[1,2]*.

[1]Department of Nuclear Science and Engineering, Massachusetts Institute of Technology, Cambridge, MA, USA

[2]Department of Materials Science and Engineering, Massachusetts Institute of Technology, Cambridge, MA, USA

[3]Honda Research Institute USA, San Jose, CA, USA

[4]Cell Design and Development Team, Rivian, Irvine, CA, USA

[5]Advanced Battery Development Team, Hyundai Motor Company, Hwaseong, 18280 Republic of Korea

[6]Department of Chemical Engineering, Changwon National University, Changwon, Gyeongsangnam-do 51140, Republic of Korea

E-mail: liju@mit.edu

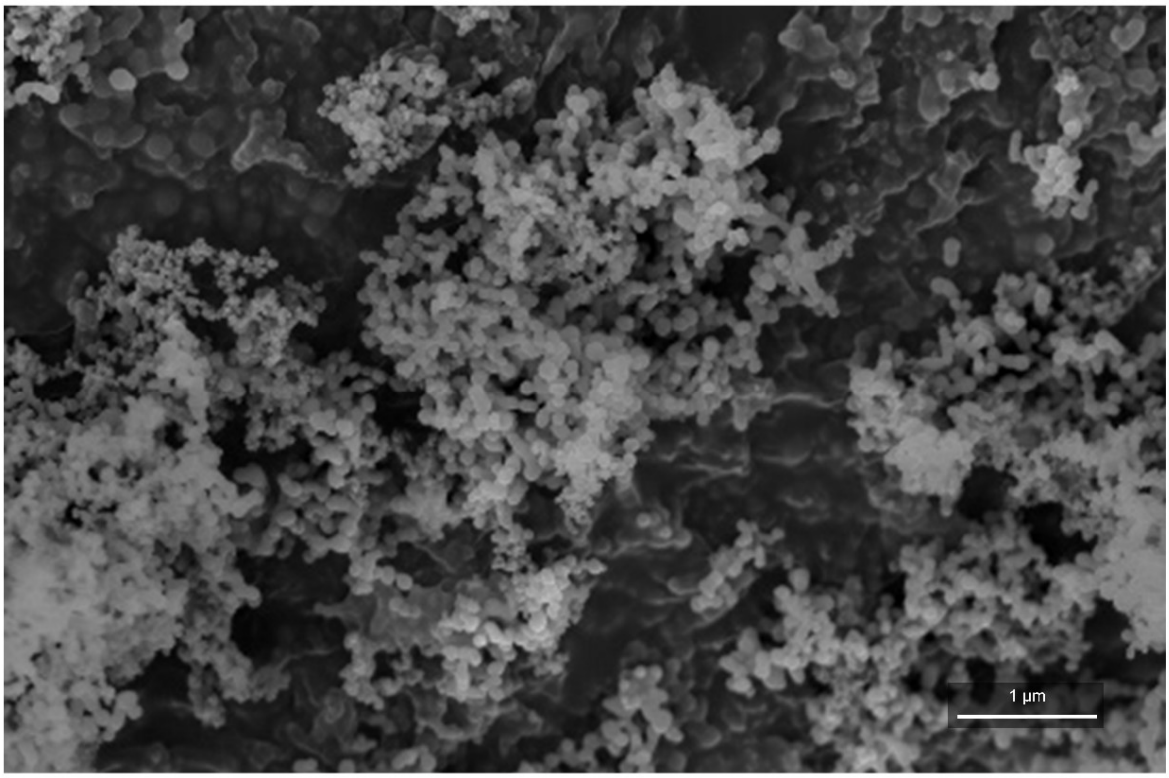

Figure S1 | SEM images (Top-view) of commercial SiNPs

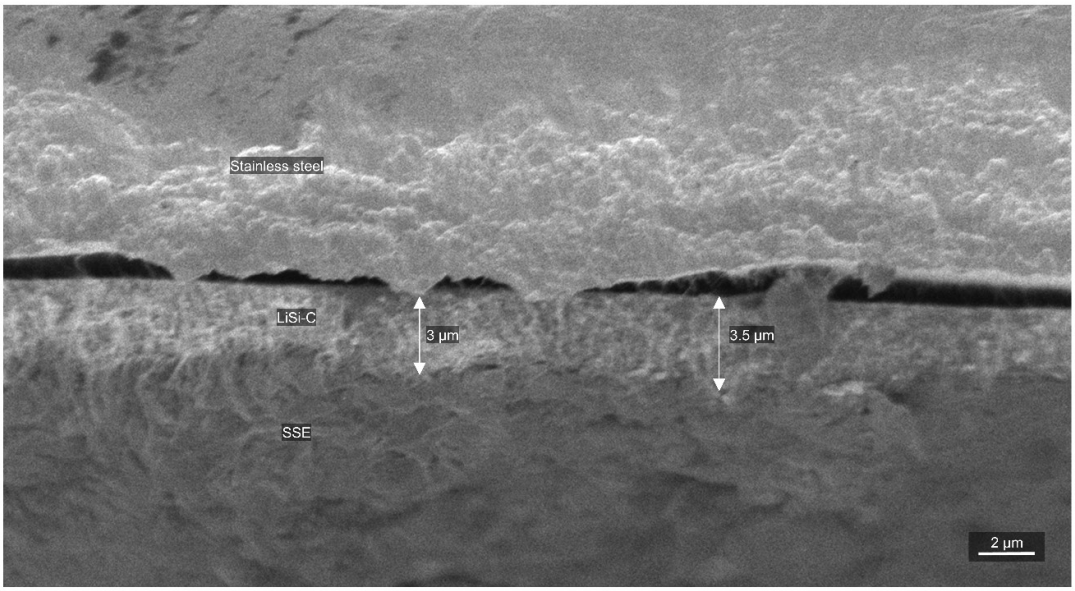

Figure S2 | Magnified cross-sectional SEM images of LiSi-C interlayer located between SSE and a stainless steel current collector.

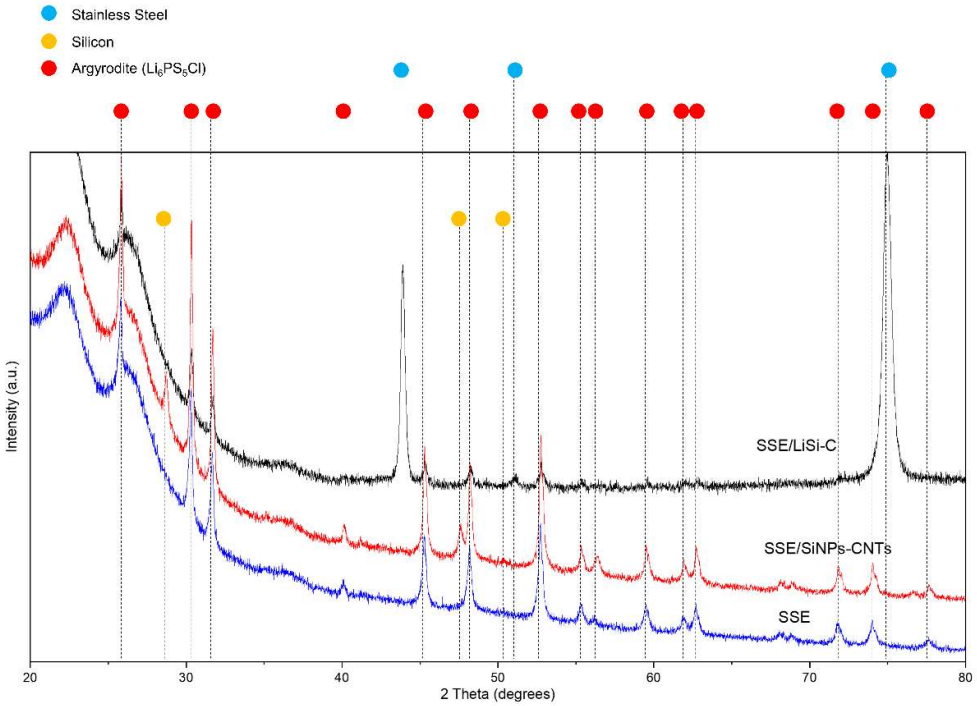

Figure S3 | XRD analysis (Cu Kα of wavelength 1.542 Å) of SSE (Li_6PS_5Cl), SSE/SiNPs-CNTs, and SSE/LiSi-C.

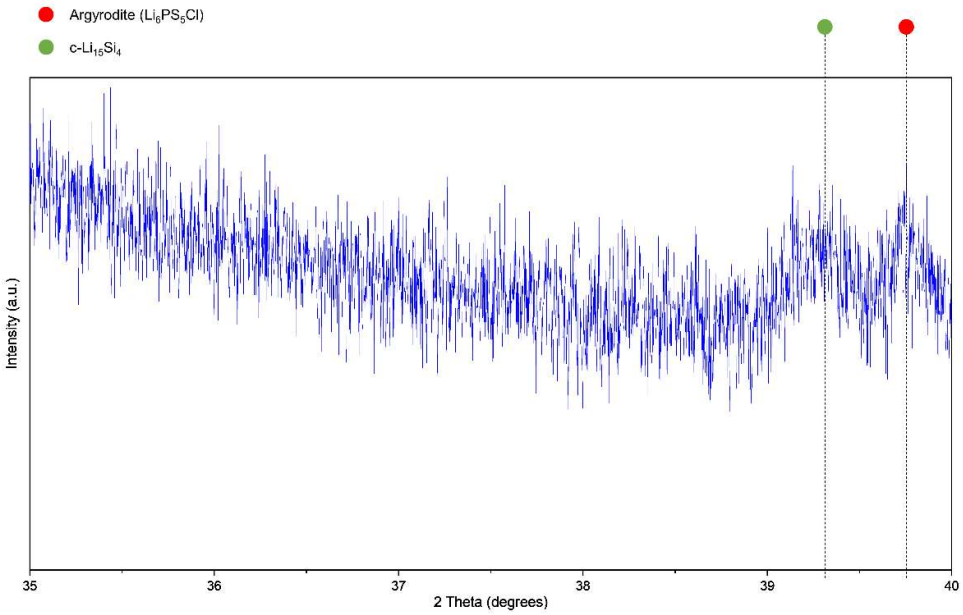

Figure S4 | XRD analysis (Mo Kα of wavelength 0.7107 Å) of SSE/LiSi-C.

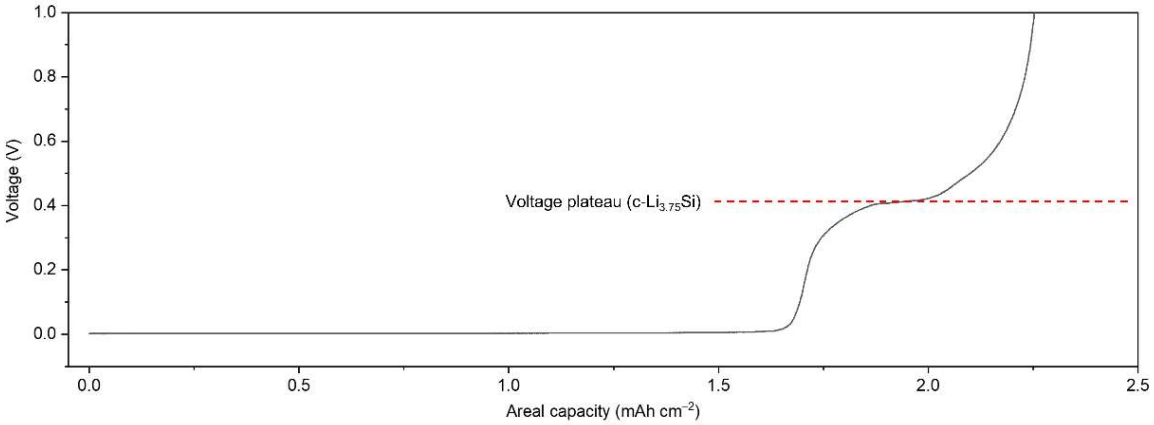

Figure S5 | Voltage profile of LiSi-C during discharging process (de-lithiation).

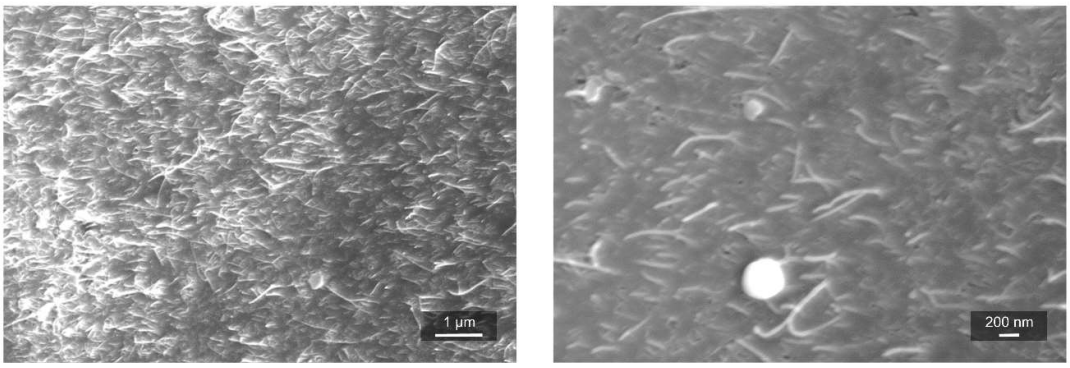

Figure S6 | Top-view of SEM image of LiSi-C surface after plating process (0.05 mAh cm^{-2})

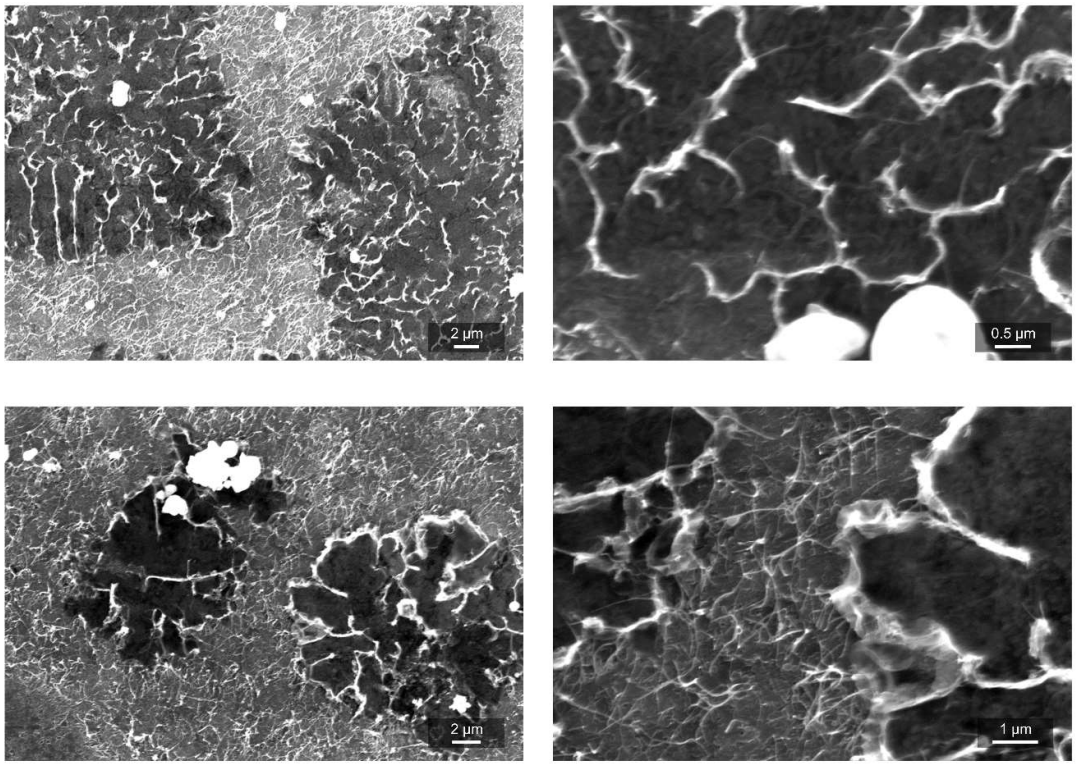

Figure S7 | Top-view of SEM image of LiSi-C surface after plating process (0.1 mAh cm^{-2})

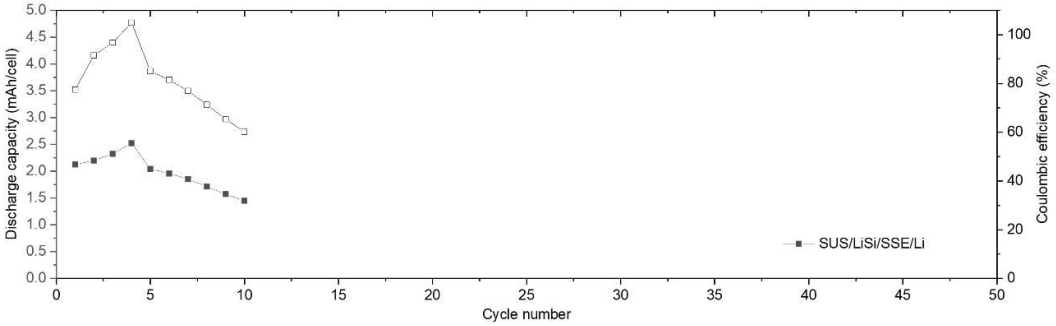

Figure S8 | Discharge capacity retention of SUS/LiSi/SSE/Li

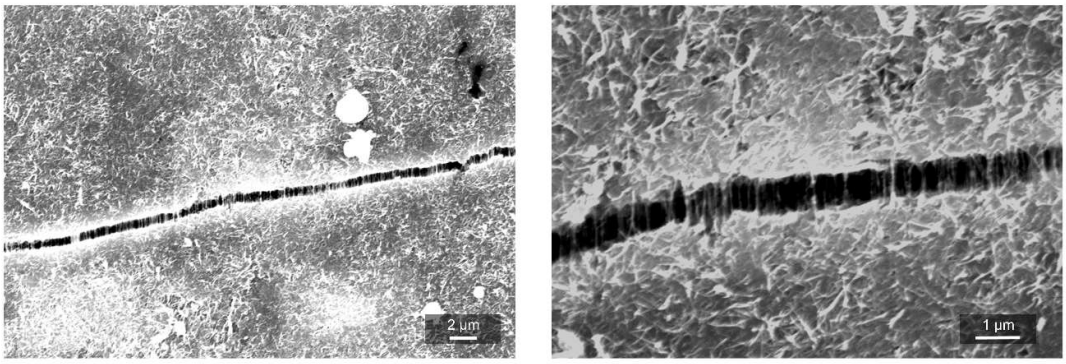

Figure S9 | Top-view of SEM image of LiSi-C after stretching and bending electrode

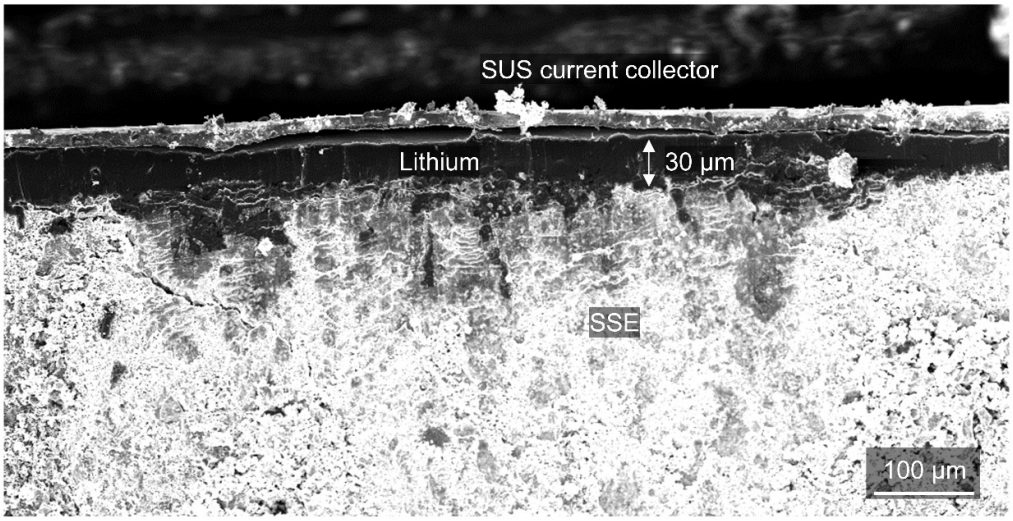

Figure S10 | Cross-sectional SEM image showing the thickness of lithium foil (30 μm) in pristine Li/Si-C/SSE/NCM811.

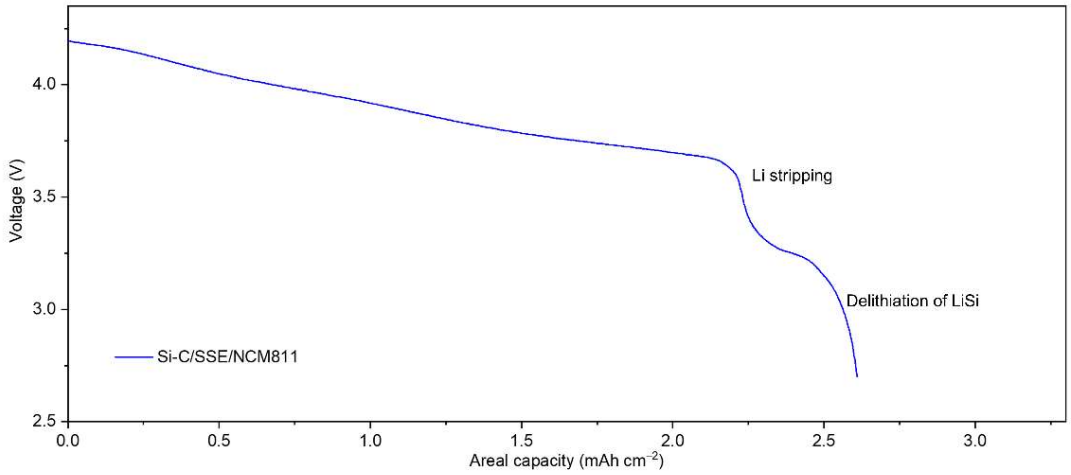

Figure S11 | Discharge voltage profiles of Si-C/SSE/NCM811 (e.g. there is no Li foil for non-electrochemical lithiation) clearly showing range of Li stripping and de-alloying reaction of LiSi at the first cycle.

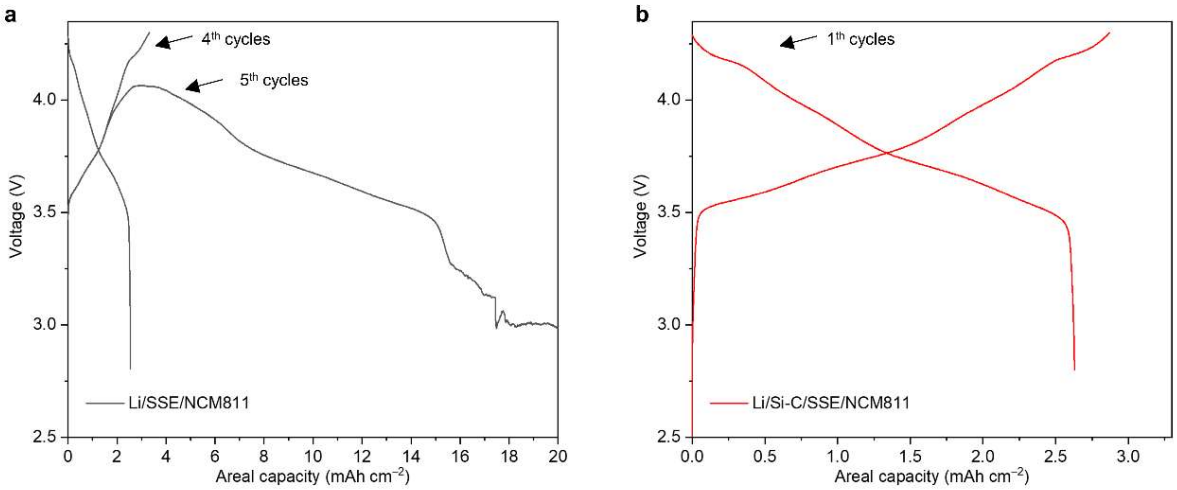

Figure S12 | Voltage profiles of Li/SSE/NCM811 (a) and Li/Si-C/SSE/NCM811 (b) at stack pressure of 64 Mpa and 5 Mpa, respectively.

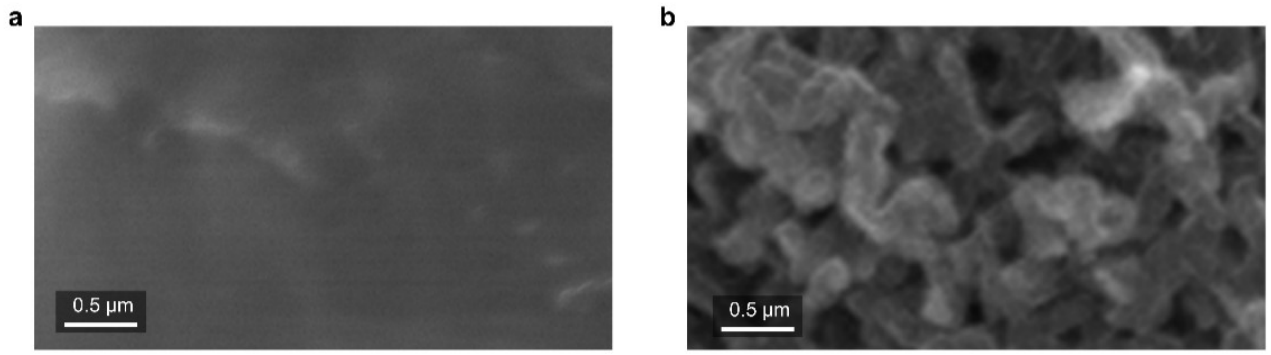

Figure S13 | Cross-sectional SEM images of Magnified lithium foil side in Li/Si-C/SSE/NCM811 (a) after 200 cycles and Li/SSE/NCM811 (b) after 73 cycles

Table S1 | Various parameters for porosity calculation of SiNPs-CNTs and LiSi-C

Porosity of SiNPs-CNTs			Porosity of LiSi-C		
True density of carbon	2.1	g/cc	True density of carbon	2.1	g/cc
Weight of carbon	0.000015	g	Weight of carbon	0.000015	g
Total volume of carbon	7.14286E-06	cc	Total volume of carbon	7.14286E-06	cc
True density of Si	2.33	g/cc	True density of LiSi	1.22	g/cc
Weight of Si	0.000135	g	Weight of LiSi (90%)	0.000260114	g
Total volume of Si	5.79399E-05	cc	Total volume of LiSi	0.000213208	cc
			Total volume of carbon	1.37626E-05	
Thickness of electrode	0.0002	cm	Thickness of LiSi	0.000325	cm
Area of electrode	0.785	cm2	Area of LiSi	0.785	cm2
Total volume of electrode	0.000157	cc	Total volume of electrode	0.000255125	cc
Volume ratio of Si MIEC	41.45399446	%	Volume ratio of LiSi	88.96446595	%
Porosity	58.54600554	%	Porosity	11.03553405	%